Transmission of $\{332\}\,\langle 113\rangle$ twins across grain boundaries in a metastable β-titanium alloy

Fengxiang Lin[a], Matthieu Marteleur[b], Pascal J. Jacques[b], Laurent Delannay[a,*]

[a] *Institute of Mechanics, Materials and Civil Engineering (iMMC-MEMA), Université catholique de Louvain, av. G. Lemaître 4, 1348 Louvain-La-Neuve, Belgium*

[b] *Institute of Mechanics, Materials and Civil Engineering (iMMC-IMAP), Université catholique de Louvain, Place Sainte Barbe 2 , 1348 Louvain-La-Neuve, Belgium*

Abstract

Plastic deformation by dislocation slip and twinning is investigated in a metastable body centered cubic Ti-Mo alloy. Experimental crystal orientation maps show twin lamellae connected across grain boundaries, especially when they host low angle misorientation angles. A three-dimensional crystal plasticity based finite element model (CPFEM) is used to predict internal stresses due to deformation twinning. It is found that twin transmission across grain boundaries relaxes the strong back-stresses at the twin tip more than dislocation slip does. CPFEM predictions also indicate that the forward-stresses, which promote twinning in the adjacent grain, depend not only on the crystal misorientation angle but also on the misorientation axis, and the inclination of the grain boundary plane.

Keywords: Crystal plasticity, twinning, residual stresses, finite element modeling, EBSD

1. Introduction

On top of enviable properties, such as low density, biocompatibility and good corrosion resistance, some titanium (Ti) alloys demonstrate excellent mechanical strength and ductility. Among them, recently developed metastable β-Ti alloys present uniform elongations larger than 35% and tensile strengths of $\sim$ 900MPa due to the progressive refinement of microstructure by martensite transformation and mechanical twinning (Marteleur et al., 2012; Sun et al., 2015). The latter microstructural changes, enhancing the work hardening ability and delaying necking, are commonly referred to as twinning-induced plasticity (TWIP) and transformation-induced plasticity (TRIP) (Grosdidier and Philippe, 2000; Ahmed et al., 2016; Castany et al., 2016). They give rise to large internal stresses which dramatically influence the elastic-plastic transients during cyclic or merely non-monotonic loading. The present paper addresses internal stresses due to twinning.

*laurent.delannay@uclouvain.be

Deformation twinning plays a particular role in the body centered cubic (bcc) β-Ti alloy. Whereas twinning of hexagonal closed packed (hcp) materials is necessary due to the low crystal symmetry and the insufficient number of (soft) dislocation slip systems, there is a competition between twinning and dislocation glide in cubic symmetry polycrystals where any plastic strain can be achieved by dislocations alone. Occurrence of twinning in bcc and face centered cubic (fcc) metals then depends on various external and internal parameters, including strain rate, deformation temperature, grain size and chemical composition of the alloys (Meyers et al., 2001). The chemical composition of β-Ti alloys determines both the stability of the β phase and the occurrence of twinning (Ahmed et al., 2016). In stable β-Ti, dislocation slip dominates. In alloys with intermediate β stability, $\{332\}\langle 113\rangle$ twinning and $\{112\}\langle 111\rangle$ twinning coexist (Bertrand et al., 2011). If the β stability further decreases, as in the alloy studied here, $\{332\}\langle 113\rangle$ twinning operates together with stress induced α'' martensite transformation (Sun et al., 2013). Because it requires additional shuffle of atoms in addition to shear, $\{332\}\langle 113\rangle$ twinning is energetically unfavorable and hence less common than $\{112\}\langle 111\rangle$ twinning (Christian and Mahajan, 1995). It is nevertheless possible to explain the prevalence of $\{332\}\langle 113\rangle$ twins for metastable β-Ti alloys. Tobe et al. (2014) considered the metastable β phase as a modulated structure with base-centered tetragonal nanodomains, due to which $\{332\}\langle 113\rangle$ twinning required a smaller magnitude of shuffle than $\{112\}\langle 111\rangle$ twinning. Lai et al. (2016) and Castany et al. (2016) rather suggested that $\{332\}\langle 113\rangle$ twinning be a follow up of α'' martensitic transformation.

Once they are formed, twin lamellae influence the subsequent plastic deformation and this can be investigated by applying continuum mechanics at the microscopic scale. In crystal plasticity theory, twinning is triggered when the shear stress resolved on a twin habit plane reaches a threshold value. The twinned region undergoes sudden shear as well as a crystal reorientation, which was first accounted for by introducing a new crystallite into the model, using the predominant twin reorientation method (Van Houtte, 1978) or a volume fraction transfer scheme (Tomé et al., 1991). The interaction of the twin with the parent grain was considered in the total Lagrangian approach (Kalidindi, 1998) whereas more recent models account also for the influence of the twin on the selection of slip systems in the parent grain (Salem et al., 2005; Proust et al., 2007; Dancette et al., 2012; Cheng and Ghosh, 2015; Wong et al., 2016). The shared idea of the latter models is that twin lamellae are obstacles reducing the mean free path of dislocations, i.e. a dynamic Hall-Petch effect (Bouaziz et al., 2008). This increases the anisotropy of individual crystals and leads to improved predictions of the macroscopic stress-strain response and the crystallographic texture evolution (Leffers and Ray, 2009). However, the amplitude of internal stresses is likely to be underestimated because such models overlook the accommodation of the transformation shear strain by the neighborhood of the twin. Clausen et al. (2008), Abdolvand et al. (2011) and Mareau and Daymond (2016) addressed internal stresses due to the accommodation of the twin shear by assuming that the parent grain is infinitely stiff, causing a large "backstress" inside the twin. More accurate predictions were obtained using spatial full-field simulations. Zhang et al. (2008) performed finite element simulations using an anisotropic yield function of the Hill type. Juan et al. (2014) introduced a double inclusion elasto-plastic self consistent model to study the effect of twin and parent domain interactions on slip system activation and hardening. According to Kumar et al. (2015), who relied on crystal plasticity and a FFT solver, the resolved shear stress that promotes twinning becomes inhomogeneous along the twin-parent interface after the redistribution of stresses due to the accommodation of the twinning strain. Abdolvand and Wilkinson (2016) used finite elements (FE) to compare the residual stresses predicted in a columnar grain microstructure to those measured by high-resolution electron backscattered diffraction (HR-EBSD). They observed high stress concentrations at the tips of twins that traversed a grain and impinged its boundaries.

A twin lamella stopped at the edge of a grain stimulates plasticity on the other side of the grain boundary, somewhat like a dislocation pile up. If twinning is initiated in the adjacent grain, it may look as if the deformation twin would propagate across the interface. If the phenomenon leads to the formation of catalytic twins or twin chains, it affects mechanical properties, such as fatigue (Yin et al., 2008) and fracture (Yang et al., 2008). Twin transmission has mostly been reported in hcp materials (Beyerlein et al., 2010; Kumar et al., 2016a) where it was found that the twin transmission probability decreases with increasing misorientation angles across the boundary. Wang et al. (2010b), Barnett et al. (2012) and Xin et al. (2015) observed that the similitude of the incoming and transmitted shear planes and shear direction is critical with regard to twin transmission, following an idea initially suggested by Luster and Morris (1995) for the transmission of dislocation slip across grain boundaries. Kumar et al. (2016a) investigated the stress concentration at the tip of a twin within a hcp tri-crystal structure, showing that an increase in plastic anisotropy enhances the probability of twin transmission. Siska et al. (2017) considered 3 ellipsoid twins in contact with each other along a line, to study mutual interaction of stress fields in hcp crystals. In contrast, there is, to the authors knowledge, no similar study in cubic metals. Whereas twins rarely transmit across grain boundaries in fcc materials, e.g. Dancette et al. (2012), some micrographs show that twins may transmit across grain boundaries in bcc β-Ti (Sun et al., 2013; Min et al., 2013). So far, most of the numerical analyses of hcp metals were performed in two dimensions, considering that the twin tip edge is perpendicular to the twin shear direction.

The crystal plasticity based finite element model (CPFEM) presented here allows three dimensional modeling of the internal stresses along all edges of a twin lamella either in the presence or in the absence of a transmitted twin lamella. The model is used to investigate the influence of twin transmission on internal stresses. We also analyze preferred conditions for twin transmission and compare model predictions to electron back-scatter diffraction (EBSD) observations of the deformed microstructure of a crystallographically textured metastable β-Ti-Mo alloy (Marteleur et al., 2012).

2. Experimental results

2.1. Initial material

A binary Ti-12wt.%Mo alloy was used in this investigation. A cast ingot was rolled at room temperature with a thickness reduction of 95%, and then annealed at 1173 K for 30 minutes followed by water quench. Before being further deformed, the fully recrystallized microstructure showed a single bcc phase, free of twins, and a mean grain size of about 50 μm.

The recrystallized material presents a strong texture. The $\{110\}$ pole figure shown in Fig. 1a was generated using the MTEX tool box (Hielscher and Schaeben, 2008) from electron backscatter diffraction (EBSD) data collected on an area of 1500 $\times$1000 μm^2. The pole figure is not perfectly orthotropic as would be expected at the mid-thickness of a rolled sheet. This is due to an insufficient texture sampling. The large grain size of the as-cast sample prevents a balanced occurrence of all variants of the texture component during the cold rolling and the subsequent recrystallization (Lin et al., 2015). The predominant lattice orientation is close to $\{634\}\langle 123\rangle$ (marked in the pole figure using open triangles), which is not far from the $\{111\}\langle 112\rangle$ orientation (open circles in the pole figure). A strong $\{111\}\langle 112\rangle$ component is common in highly rolled and recrystallized low-carbon steel with bcc symmetry (Hölscher et al., 1991). The $\{111\}\langle 112\rangle$ texture was also observed in a β-Ti alloy after 90% warm rolling and recrystallization (Sander and Raabe, 2008).

The distribution of the misorientation angle across grain boundaries is shown in Fig. 1b. When compared to a random texture, the present material contains a widely scattered distribution of misorientation angles. About 33% of the grain boundaries have misorientations lower than 15°.

2.2. Twinning during a uniaxial tensile test

The recrystallized samples underwent uniaxial tension along the rolling direction. After only 1% elongation, twinning was already observed in some grains. As the tensile strain increased, twinning occurred in a larger proportion of grains, and both the number of twins and their volume fraction increased inside individual grains. The EBSD orientation map in Fig. 2 shows the microstructure after 5% tensile strain,

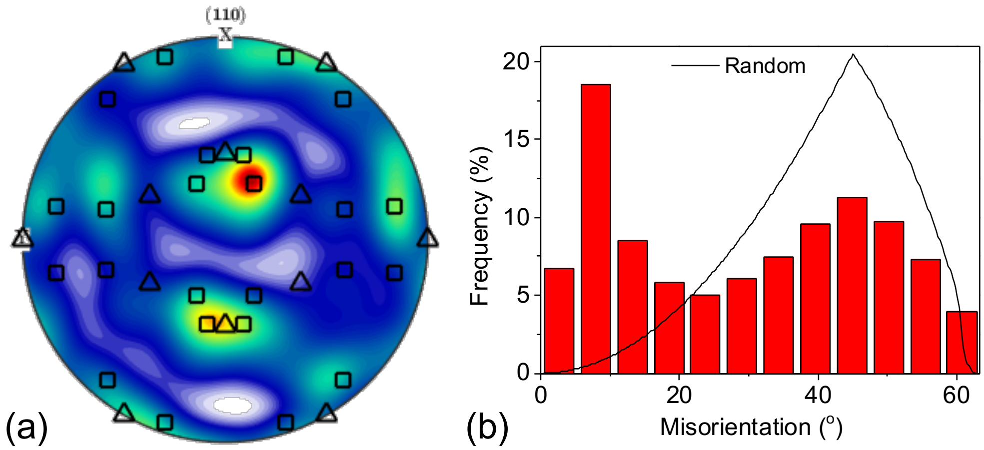

Figure 1: {110} pole figure showing the recrystallized texture (a) and the distribution of the grain boundary misorientations in the recrystallized material.

when twin lamellae cover about 20% of the sample area. Table 1 lists the Euler angles of individual grains in Fig. 2 as well as the Schmid factors (SF) of the observed twins. The latter SF is computed assuming that the macroscopic uniaxial tensile stress applies uniformly inside all grains. The tensile direction is horizontal in the figure. Inside most of the grains, the twin variant with the highest SF dominates, and a second or third twin variant with lower SF is observed only near the grain boundary. In grain Gr11, two variants with the largest and second largest SF intersect each other. The twin and matrix crystal orientations indicate that the active twinning system is always $\{332\}\langle 113\rangle$. Twins have a lamellar shape, with the twin/matrix interfaces roughly parallel to a $\{332\}$ crystallographic plane. Consistent with the low stability of the β phase (Marteleur et al., 2012), the $\{112\}\langle 111\rangle$ twinning mode has been scarcely observed in the orientation maps and will hence not be accounted for in the present study.

In the orientation maps, we observe many adjoining twin pairs (ATPs) connected across a grain boundary. In principle, such ATPs could arise in three situations:

- Twinning occurs in a single grain which, as a result of heterogeneous plastic deformation, is subsequently subdivided in two subregions with a moderate lattice misorientation.
- Two twins nucleate simultaneously at the grain boundary, and then propagate into the bulk of the two grains.
- One of the two twins forms first, and propagates across the grain until it reaches the boundary and triggers twinning in the adjacent grain.

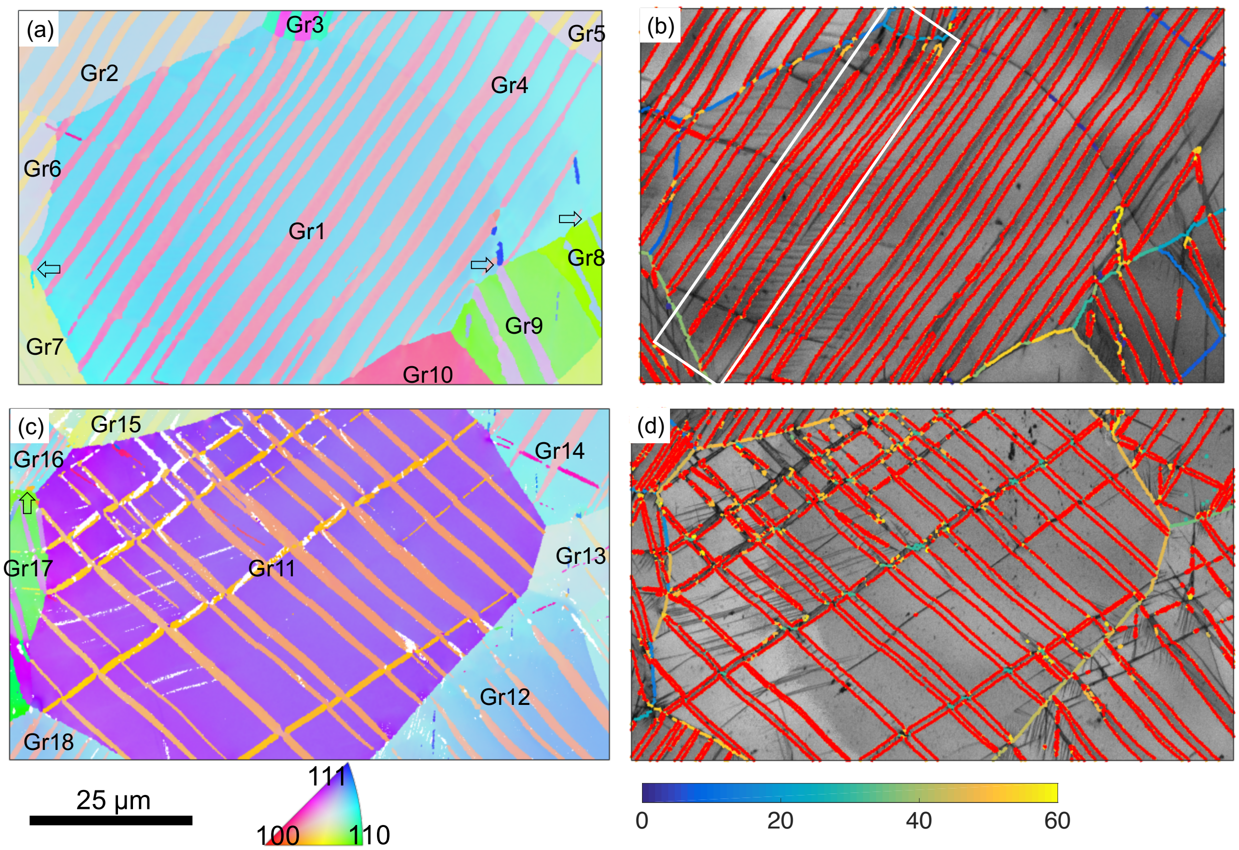

Figure 2: EBSD maps showing the microstructure after 5% elongation. (a) and (c) Maps colored according to the crystallographic orientation of the tensile direction. The tensile direction is horizontal. Grain numbers are marked. (b) and (d) Maps of the EBSD band contrast. Grain boundaries are shown in color varying according to the misorientation angles. Twin boundaries are shown in red. The white rectangle marks a region where twin lamellae are curved, and this region is enlarged in Fig. 4.

Table 1: Crystal orientations shown in Fig 2 and Schmid factor (SF) for uniaxial tension of the observed twins.

Grain No	Euler angle	SF
Gr1	[156, 130, 215]	0.49/0.36/0.12
Gr2	[152, 142, 213]	0.48
Gr3	[161, 146, 207]	0.47
Gr4	[156, 133, 215]	0.49/0.14
Gr5	[157, 133, 223]	0.47
Gr6	[156, 134, 221]	0.48/0.38
Gr7	[192, 153, 221]	0.41/0.30
Gr8	[179, 139, 215]	0.37/0.38
Gr9	[189, 149, 224]	0.42
Gr10	[343, 147, 240]	–
Gr11	[50, 41, 19]	0.47/0.44/0.26
Gr12	[208, 46, 33]	0.49
Gr13	[198, 43, 44]	0.46
Gr14	[150, 35, 63]	0.49/0.35
Gr15	[163, 30, 45]	0.43
Gr16	[151, 36, 62]	0.49
Gr17	[188, 40, 33]	0.43/0.32/0.12
Gr18	[140, 32, 72]	0.49

The first situation is excluded here, considering that twins were absent in the recrystallized sample and that the 5% elongation of the tensile test is insufficient to induce such sharp subgrain boundaries. The second situation is difficult to assess as the EBSD map offers only a snapshot of the deformation process. The third situation, twin transmission, is more probable at least in those cases where we observe twin lamellae chained to go across more than two grains. In the sequel, we consider for simplicity that all ATPs are the result of twin transmission but the conclusions of the analysis remain valid if the two twin lamellae would rather have originated simultaneously at a stress concentration along the grain boundary.

Table 2 describes the twin transmission situations observed in Fig. 2 using several parameters. The first five grain boundaries are easily transmitted through. Almost every impinging twin lamella propagates into the entire adjacent grain without obvious change of the twin thickness. Such boundaries tend to present low misorientation angles. In Table 2, the next four grain boundaries are not systematically traversed. Only a few of the incoming twins are transmitted and they do not propagate much inside the adjacent grain. Another twin variant dominates in the central part of the latter grain. These occasionally transmitted twins are marked in Fig. 2 by arrows. The next two lines in the table correspond to two grains boundaries where the transmission is unclear, since it is difficult to determine whether or not the two set of twins are connected with each other at the grain boundary. Finally, transmission was never observed across the last eight boundaries listed in Table 2. The general trend is that the larger the misorientation angle is, the lower the chances for twin transmission. However, the grain boundaries Gr1/Gr3, Gr16/Gr17 and Gr8/Gr4 all have misorientation angles around 20°, but twin transmission is different for each one of them.

In the literature (Wang et al., 2010b; Barnett et al., 2012; Xin et al., 2015), it has been suggested that twin transmission occurs when there is a small misalignment of the two twin plane normals and the two twin shear directions. Calling θ_n and θ_b the two misalignment angles, the geometrical compatibility factor, which measures the similitude of the two twinning systems, has been defined as:

$$m' = (\vec{b}_{tw} \cdot \vec{b'}_{tw})(\vec{n}_{tw} \cdot \vec{n'}_{tw}) \;=\; \cos(\theta_b)\;\cos(\theta_n) \tag{1}$$

where $\vec{b'}_{tw}$ and $\vec{n'}_{tw}$ refer to a twin system in the grain adjacent to the incoming twin lamella. In Table 2, all boundaries across which twins are systematically transmitted have $m' > 0.9$ and both twins in those ATP, have a SF larger than 0.47. This indicates that both grains are equally likely to undergo twinning and it is difficult to identify which one is the incoming twin. For the boundaries which impinging twins occasionally traverse, the incoming twin has high SF but the transmitted twin has a lower SF, and sometimes is only the second or third most favorable twin variant. However, the transmitted twin systematically is the variant

Table 2: Misorientations and twin transmission situations across grain boundaries in Fig. 2. The Schmid fator of the incoming and transmitted twins (SF), the geometrical compatibility factor (m') and the angles θ_b and θ_n of misalignment of two twinning systems are also listed. For grain boundaries where the incoming twin is constrained, twin variants in the neighboring grain with the highest SF and with the highest m' are listed, and marked with underlines.

GB	Misorientation	Transmission	SF	m'	θ_n	θ_b
Gr1/Gr4	3°	Systematic	0.49/0.49	1.00	2°	3°
Gr1/Gr6	6°	Systematic	0.49/0.48	0.99	3°	6°
Gr4/Gr5	7°	Systematic	0.49/0.47	0.99	6°	3°
Gr1/Gr2	12°	Systematic	0.49/0.48	0.98	5°	11°
Gr1/Gr3	21°	Systematic	0.49/0.47	0.93	19°	11°
Gr16/Gr17	22°	Occasional	0.49/0.32	0.86	22°	19°
Gr8/Gr4	24°	Occasional	0.37/0.14	0.87	22°	19°
Gr9/Gr1	33°	Occasional	0.42/0.12	0.77	24°	32°
Gr1/Gr7	39°	Occasional	0.47/0.30	0.71	38°	26°
Gr11/Gr17	47°	Unclear	0.47/0.12	0.58	31°	47°
Gr11/Gr15	49°	Unclear	0.44/0.43	0.3	69°	35°
Gr18/Gr17	28°	No	0.49/$\underline{0.43}$	$\underline{-0.06}$		
			0.49/$\underline{0.33}$	$\underline{0.80}$		
Gr13/Gr14	36°	No	0.47/$\underline{0.49}$	$\underline{-0.03}$		
			0.47/$\underline{0.44}$	$\underline{0.71}$		
Gr11/Gr12	39°	No	0.43/$\underline{0.49}$	$\underline{0.16}$		
			0.43/$\underline{0.25}$	$\underline{0.74}$		
Gr11/Gr13	45°	No	0.44/$\underline{0.46}$	$\underline{0.11}$		
			0.43/$\underline{0.12}$	$\underline{0.64}$		
Gr11/Gr16	46°	No	0.43/$\underline{0.49}$	$\underline{0.35}$		
			0.43/$\underline{0.35}$	$\underline{0.70}$		
Gr11/Gr14	47°	No	0.47/$\underline{0.49}$	$\underline{0.70}$		
Gr11/Gr18	52°	No	0.44/$\underline{0.49}$	$\underline{0.35}$		
			0.44/$\underline{0.35}$	$\underline{0.70}$		
Gr1/Gr10	54°	No	0.49/$\underline{0.37}$	$\underline{0.04}$		
			0.49/$\underline{0.08}$	$\underline{0.53}$		

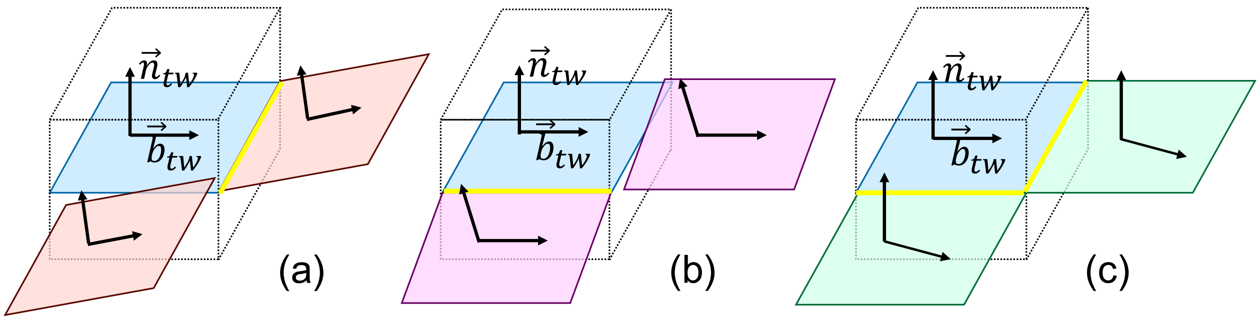

Figure 3: Influence of the lattice misorientation on the line of contact of the incoming and transmitted twin lamellae. The thick yellow lines highlight twin edges that allow transmission along a line within the grain boundary. Three lattice misorientation axes are considered: (a) $\vec{b}_{tw} \times \vec{n}_{tw}$, (b) $\vec{b}_{tw}$, and (c) $\vec{n}_{tw}$.

that holds the highest m' value (> 0.7 for the present four grain boundaries). The twin variants with the largest SF dominate in the central part of the adjacent grains. For the boundaries impinged by an incoming twin lamella that is not transmitted, all twelve twin variants of the adjacent grain have either a low m' value or a low SF value. For these boundaries, Table 2 provides the m' and SF values for the two most likely (and yet unobserved) ATPs. A third orientation map covering a larger number of grains is analyzed in the Appendix. The latter EBSD measurements were performed at a larger strain (about 8% elongation), impeding the indexation of lattice orientations inside the twins. Twin variants were hence identified based on the traces of habit planes and the trends observed in Fig. 2 were confirmed.

The previous analysis might overlook an important supplementary condition for twin transmission: the two twin lamellae are adjoining in 3D only if the line of intersection of the twin planes lies inside the grain boundary. This is illustrated in Fig. 3 where three idealized cases are considered: the incoming twin lies inside a cubic grain and the lattice misorientation with regard to adjacent grains is around, respectively, $\vec{b}_{tw}$, $\vec{n}_{tw}$, and $\vec{b}_{tw} \times \vec{n}_{tw}$. We observe that twin transmission is theoretically possible only along those edges of the twin lamella that are parallel to the axis of the lattice misorientation. The only exception is if the incoming and transmitted twins are co-planar, i.e. if the lattice misorientation axis is $\vec{n}_{tw}$. In a three dimensional microstructure with irregular and equi-axed grain shapes, chances are scarce that the incoming and transmitted twins meet exactly along a line inside the grain boundary. Indeed, in bcc crystals, the adjacent grains each have only twelve twinning planes and only few have a large SF.

The rather large number of ATPs observed experimentally is explained by the large proportion of low angle misorientation boundaries (Fig. 1b) and also by the fact that some twin lamellae deviate from the coherent $\{332\}$ plane. The topology of ATPs was not probed in 3D. This would have required serial sectioning of the sample and multiple EBSD maps (Rohrer et al., 2010). However, as a single EBSD map provides a random sampling of the 3D microstructure, ATPs observed in a 2D section are likely to remain adjoining

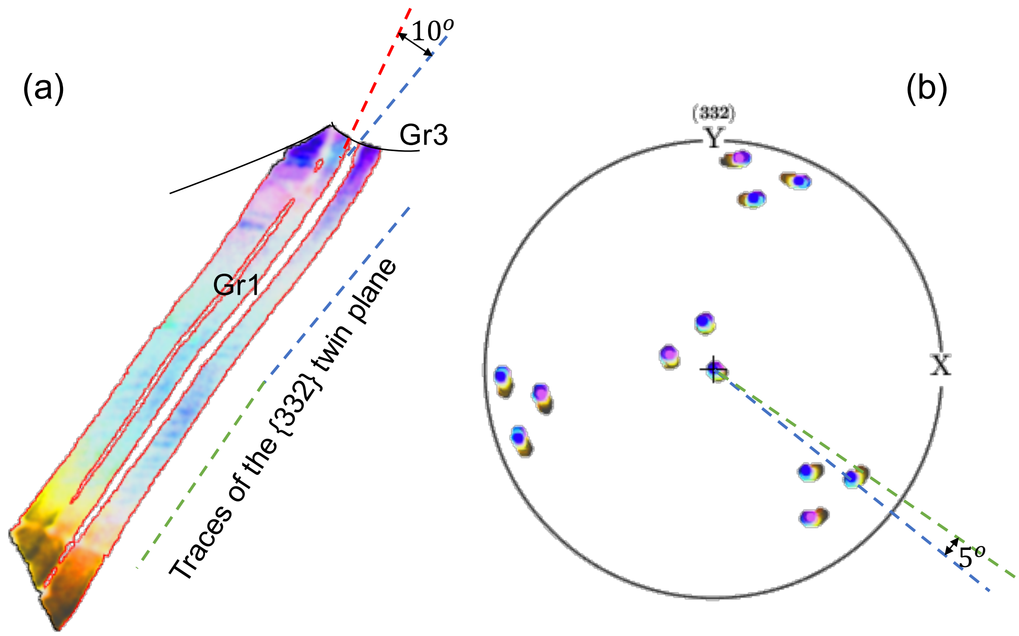

Figure 4: (a) Close up on curved twin lamellae (region in the white rectangle in Fig. 2). The two parallel twin lamellae are white regions surrounded by red boundaries, and the matrix is colored to show the orientation spread in the {332} pole figure presented in (b). The dashed lines highlight the curvatures of the twin lamellae and of the crystal lattice. The {332} crystal plane is represented by its trace in (a) and by its normal in (b).

within a 3D volume outside the section. The region inside the white rectangle in Fig. 2b is enlarged in Fig. 4a, showing twinned regions in white whereas the parent grain is colored in the same way as the {332} pole figure presented in Fig. 4b. As a result of heterogeneous dislocation slip, the parent grain hosts a lattice orientation spread of about 5°, developing from the bottom left corner to the top right corner of Fig. 4a. The trace of the {332} plane in the parent grain is easily derived from the pole figure: it is perpendicular to the line connecting the center of the pole figure to the local {332} pole. When travelling from the bottom-left to the top right-corner of Gr1, the trace of {332} rotates clockwise (from the green dashed line to the blue dashed line). Interestingly, the interface with the twin lamellae conforms to the curvature of the {332} plane in the bulk of Gr1 but it rotates anti-clockwise when approaching the grain boundary, so as to connect to the adjoining twin lamellae in Gr3. Inside the bulk of Gr1, the twin/matrix interface hosts a misorientation which is within 2° from the ideal {332} ⟨113⟩ relationship. Such misorientation is represented by a red line in Fig. 4a. Nearby the Gr1/Gr3 boundary, the twin/matrix interfaces deviates by about 10° relative to the {332} crystal plane (marked by a blue dashed line). Without the latter deviation, the twin lamellae in Gr1 would not connect to those in Gr3.

3. Crystal plasticity simulations

The numerical modeling is conducted on a 3D polycrystalline aggregate. It is aimed at estimating the internal stresses developed inside and around a newly formed twin lamella as well as the partial stress relaxation when twinning is initiated in an adjacent grain, creating an adjoining twin pair (ATP).

3.1. *Model description*

The geometry of the two lamellae forming the ATP under investigation is determined a priori and it is presented in Fig. 5. The ATP is placed at the center of a polycrystal in which the 64 constitutive grains form a periodic Voronoi tessellation. The twin lamellae of the ATP extend through the entire hosting grains (Fig. 5b). Their thickness leads to an aspect ratio of about 13 and it represents about 5% of the volume in the hosting grains. The two twin planes are inclined by 13° relative to each other. They intersect along a straight segment which is inside the planar boundary between the two adjacent grains. The contact area of the two twin lamellae is a thin rectangular facet in this boundary. The polycrystal is embedded inside a uniform matrix forming a cube with edges ten times larger than the size of the polycrystal. The uniform matrix acts as a buffer layer that minimizes the influence of boundary conditions on the stress field nearby the twin lamellae, which is the focus of interest. The uniform matrix deforms according to isotropic J_2 elasto-plasticity and its stiffness, strength and linear hardening, $\sigma_y = \sigma_{y0}(1 + \varepsilon/\varepsilon_0)$, mimic the response of the polycrystal so that deformation is evenly distributed between the matrix and the polycrystal.

The lattice orientations of the two grains hosting twins are prescribed in such a way that the lamellae are parallel to $\{332\}$ crystal planes whereas the twin shear directions $\langle 113 \rangle$ are in both grains either parallel or perpendicular to the grain boundary. With such orientations, no misalignment needs to be compensated by forming incoherent twin boundaries. The situation that both $\vec{b}_{tw}$ and $\vec{b'}_{tw}$ are perpendicular to the grain boundary corresponds to a misorientation between the two grains around the axis of $\vec{b}_{tw} \times \vec{n}_{tw}$, similar to that shown in Fig. 3a. The situation that both $\vec{b}_{tw}$ and $\vec{b'}_{tw}$ are parallel to the grain boundary corresponds to a misorientation between the two grains around the axis of $\vec{b}_{tw}$, similar to that shown in Fig. 3b. These two situations are later referred to as $\vec{b}_{tw} \times \vec{n}_{tw}$ and $\vec{b}_{tw}$ types. The lattice orientations of the 62 other grains are selected randomly while it has been verified that the results presented next do not vary much when a simulation is repeated using different random orientations samplings, or when assigning grain orientations representative of the texture measured experimentally.

A finite element mesh conforming to the microstructure is generated using the gmsh library (Kowalski

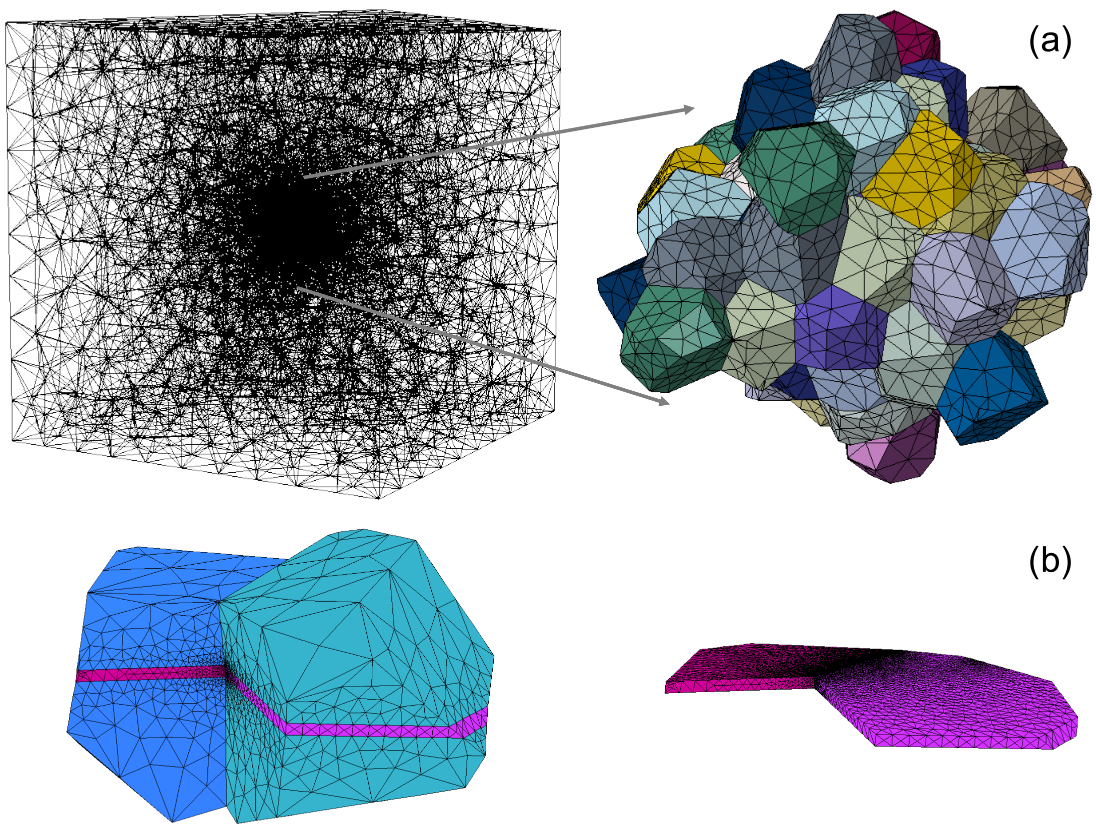

Figure 5: Representation of the grain geometry used for the FE simulation. (a) The uniform matrix and the 3D polycrystal structure. (b) The two grains with a prescribed adjoint twin pair (ATP).

et al., 2016). Each grain is discretized into about 400 second-order tetrahedral elements (C3D10 in ABAQUS) and the mesh is further selectively refined at the edges of the twin lamellae, i.e. where we expect the development of large internal stresses during twinning. Displacements are prescribed incrementally at all nodes of the cube faces. The boundary conditions enforce that the cube faces remain flat and they warrant that the volume average of the stress tensor is uniaxial. However, the tensile axis does not correspond to an edge of the cube. In order to ensure that twinning of the ATP is likely to occur, the tensile axis is tilted at about 45° relative to the twin lamellae, which maximizes the resolved shear stress τ_{tw} on the twinning system in each grain, i.e. the Schmid factor for twinning is large in both lamellae.

A user-defined material law (UMAT routine) implements crystal plasticity theory in the ABAQUS finite element code (Delannay et al., 2009; Dancette et al., 2012; Amodeo et al., 2016). The constitutive law is integrated fully implicitly within a reference frame rotating with the crystal lattice. For this, the deformation gradient tensor, $\boldsymbol{F} = \boldsymbol{R}^{\star}\boldsymbol{U}^{\mathrm{el}}\boldsymbol{F}^{\mathrm{p}}$, is multiplicatively decomposed into a lattice rotation $\boldsymbol{R}^{\star}$, an infinitesimal elastic stretch such that $\left\|\boldsymbol{U}^{el} - \boldsymbol{I}\right\| \ll 1$, and a transformation $\boldsymbol{F}^{\mathrm{p}}$ resulting from dislocation slip and twinning. Using a dot to represent time derivatives, the velocity gradient tensor is approximated as follows:

$$\begin{aligned} \boldsymbol{L} = \dot{\boldsymbol{F}}\boldsymbol{F}^{-1} &= \boldsymbol{R}^{\star}\left(\boldsymbol{R}^{\star T}\dot{\boldsymbol{R}}^{\star} + \dot{\boldsymbol{U}}^{\mathrm{el}}\boldsymbol{U}^{\mathrm{el}^{-1}} + \boldsymbol{U}^{\mathrm{el}}\dot{\boldsymbol{F}}^{\mathrm{p}}\boldsymbol{F}^{\mathrm{p}-1}\boldsymbol{U}^{\mathrm{el}^{-1}}\right)\boldsymbol{R}^{\star T} \\ &\simeq \boldsymbol{R}^{\star}\left(\boldsymbol{R}^{\star T}\dot{\boldsymbol{R}}^{\star} + \dot{\boldsymbol{U}}^{\mathrm{el}} + \dot{\boldsymbol{F}}^{\mathrm{p}}\boldsymbol{F}^{\mathrm{p}-1}\right)\boldsymbol{R}^{\star T} \end{aligned} \tag{2}$$

Hence, the velocity gradient is the sum of three tensors rotating with the crystal lattice. In the sequel, a tilde is adjoined above all such co-rotational vectors and tensors, which includes the (anisotropic) elastic stiffness tensor $\widetilde{\boldsymbol{\mathcal{C}}}$, and the plastic velocity gradient $\widetilde{\boldsymbol{L}}_{\mathrm{p}} = \dot{\boldsymbol{F}}^{\mathrm{p}}\boldsymbol{F}^{\mathrm{p}-1}$. At any given time step, the crystal is assumed to undergo either dislocation slip or twinning, not both, i.e. dislocation slip is switched off inside the lamellae when they are twinning. This is justified if we consider that twinning occurs suddenly.

In regions where dislocation glide operates, the slip rates $\dot{\gamma}_k$ are computed using the conventional viscoplastic power-law proposed by Hutchinson (1977):

$$\widetilde{\boldsymbol{L}}_{\mathrm{p}} = \sum_k \widetilde{\boldsymbol{M}}_k \dot{\gamma}_k = \sum_k \widetilde{\boldsymbol{M}}_k \dot{\gamma}_0 \left|\frac{\widetilde{\boldsymbol{M}}_k : \widetilde{\boldsymbol{\sigma}}}{\tau_c}\right|^{1/m} sign\left(\widetilde{\boldsymbol{M}}_k : \widetilde{\boldsymbol{\sigma}}\right) \tag{3}$$

$\dot{\gamma}_0$ is the reference slip rate, m is a very low rate sensitivity exponent and the Schmid tensor $\widetilde{\boldsymbol{M}}_k = \widetilde{\boldsymbol{b}}_k \otimes \widetilde{\boldsymbol{n}}_k$ is the diadic product of the slip plane normal $\widetilde{\boldsymbol{n}}_k$ and the normalized Burgers' vector $\widetilde{\boldsymbol{b}}_k$. It is assumed that dislocation slip occurs along 24 slip systems of the $\{110\}\langle 111\rangle$ and $\{112\}\langle 111\rangle$ types. The common critical resolved shear stress τ_c evolves proportionally to the accumulated dislocation slip:

$$\tau_c = \tau_{c0}\left(1 + \frac{\Gamma}{\Gamma_0}\right) \quad \text{where } \Gamma = \int_0^t \sum_k \left|\dot{\gamma}^k\right| dt \tag{4}$$

During twinning of the ATP, the plastic velocity gradient is adapted (only inside the finite elements forming the lamellae): equation (3) is replaced by:

$$\widetilde{\boldsymbol{L}}_{\mathrm{p}} = \left(\widetilde{\boldsymbol{b}}_{tw} \otimes \widetilde{\boldsymbol{n}}_{tw} + \boldsymbol{\Omega}_{tw}\right)\, \dot{\gamma}_{tw} \tag{5}$$

Here $\widetilde{\boldsymbol{n}}_{tw}$ is the twin plane normal, $\widetilde{\boldsymbol{b}}_{tw}$ is the twin shear direction, $\boldsymbol{\Omega}_{tw}$ is a skew-symmetric tensor representing a rotation around $\widetilde{\boldsymbol{n}}_{tw}$, and $\dot{\gamma}_{tw}$ is a twinning rate, which is prescribed long enough to achieve the shear strain (0.3536 for $\{332\}\,\langle 113\rangle$ twinning) and the lattice reorientation expected after complete twinning. The finite element simulation is decomposed in two stages. The material is first preloaded while allowing only dislocation slip throughout the polycrystal. Then, twinning of one or both lamella(e) of the ATP is enforced while maintaining the macroscopic stress state constant, i.e. while preserving uniaxial tension on average over the mesh.

The six components of $\widetilde{\boldsymbol{\sigma}}$ and the three components of the lattice spin $\dot{\widetilde{\boldsymbol{\Omega}}}^{\star} = \boldsymbol{R}^{\star T}\dot{\boldsymbol{R}}^{\star}$ are computed by integrating the following tensorial equation in which $\overline{\boldsymbol{L}}$ is the latest estimate of the local velocity gradient computed by Abaqus:

$$\widetilde{\boldsymbol{\mathcal{C}}}^{-1} : \dot{\widetilde{\boldsymbol{\sigma}}} + \dot{\widetilde{\boldsymbol{\Omega}}}^{\star} + \widetilde{\boldsymbol{L}}_{\mathrm{p}} - \boldsymbol{R}^{\star T}\,\overline{\boldsymbol{L}}\,\boldsymbol{R}^{\star} = 0 \tag{6}$$

The fully-implicit time integration adopts a Newton-Raphson iterative solution. Then, a consistent tangent operator is provided to the finite element solver, while accounting for the following relationship linking the co-rotational stress $\widetilde{\boldsymbol{\sigma}}$ to the Cauchy stress $\boldsymbol{\sigma}$ expressed in a fixed frame common to all crystals:

$$\dot{\widetilde{\boldsymbol{\sigma}}} = \dot{\boldsymbol{\sigma}} - \dot{\widetilde{\boldsymbol{\Omega}}}^{\star}\boldsymbol{\sigma} + \boldsymbol{\sigma}\dot{\widetilde{\boldsymbol{\Omega}}}^{\star} \tag{7}$$

The material parameters are listed in Table 3. The elastic constants for the investigated Ti-Mo alloy are extrapolated from the values reported in (Welsch et al., 1993). The parameters τ_{c0}, Γ_0, σ_{y0} and ε_0 fit the initially constant hardening rate of the tensile curve reported in (Marteleur et al., 2012).

Table 3: Material parameters used in FE simulations

polycrystal	C_{11} (GPa)	C_{12} (GPa)	C_{44} (GPa)	τ_c (MPa)	Γ_0	$\dot{\gamma}_0$ (s^{-1})	m
	125	100	41	170	1.32	0.001	0.02
buffer	E (GPa)	ν		σ_y (MPa)	ε_0		
	78	0.37		481	0.64		

3.2. *Predictions of the evolution of internal stresses with and without twin transmission*

The ATP and the 2D cuts of the two neighboring grains with the prescribed ATP are presented in Fig. 6. One of the grains is termed grain N0, and is assigned to have the highest Schmid factor for twinning, i.e. it is the grain that is selected to host the first twin lamella. The other grain is termed grain N1. The internal stresses due to twinning are largest in the close vicinity of the twin edges. Their average value is probed inside a tubular region that contains all material points located at a short distance from the linear intersection of the twin plane and the grain boundaries. It is computed by accounting for the distance d_{out} of each point to its projection on the twin plane as well as the distance d_{in} of the projection to the nearest twin edge. A material point is considered sufficiently close to the twin edge if $d_{in}^2 + (d_{out}/2)^2 \leq (t/2)^2$ where t is the thickness of the twin lamella. With this definition, the twin tip regions tend to match the regions with high stress concentration. The twin tip region in grain N0 near the twin edge between the prescribed two twins is termed Ω_0, and the twin tip in grain N1 is termed Ω_1. Each one is a half tubular region, as indicated in Fig. 6. Fig. 6b shows grain N0 and N1 viewed in the section perpendicular to the twin edge (termed twin edge view). The twin edge view is similar to the geometry used in most of the published 2D or quasi-2D simulations (Kumar et al., 2016b). Fig. 6c shows the two twin lamellae cut at the mid-thickness of the twin (termed twin plane view). It should be noted that the cutting sections through the twins in grain N0 and N1 are not the same, because the twin planes of the two twins are inclined from each other by 13°.

Simulations proceeded in two steps. The preloading step in uniaxial tension occurred without twinning until a true elongation of 2% (corresponding to a tensile stress of around 490 MPa). During the subsequent step, the macroscopic stress was held constant and twinning was enforced (by applying Eq. (5)) either only inside the lamella of grain N0 or inside both twin lamellae. The former corresponds to the situation where twinning is constrained by the grain boundary, whereas the latter corresponds to the situation where twin transmission occurs. The total amount of shear prescribed inside each lamella was 0.3536 as expected from mechanical twinning in this material.

The simulation was carried out twice while changing the twin shear direction. The macroscopic tensile direction was adapted to warrant the same high resolved shear stress for twinning (τ_{tw}) in both simulations. In the first simulation ($\vec{b}_{tw} \times \vec{n}_{tw}$ type), the twin shear direction $\vec{b}_{tw}$ in both grains was perpendicular to the

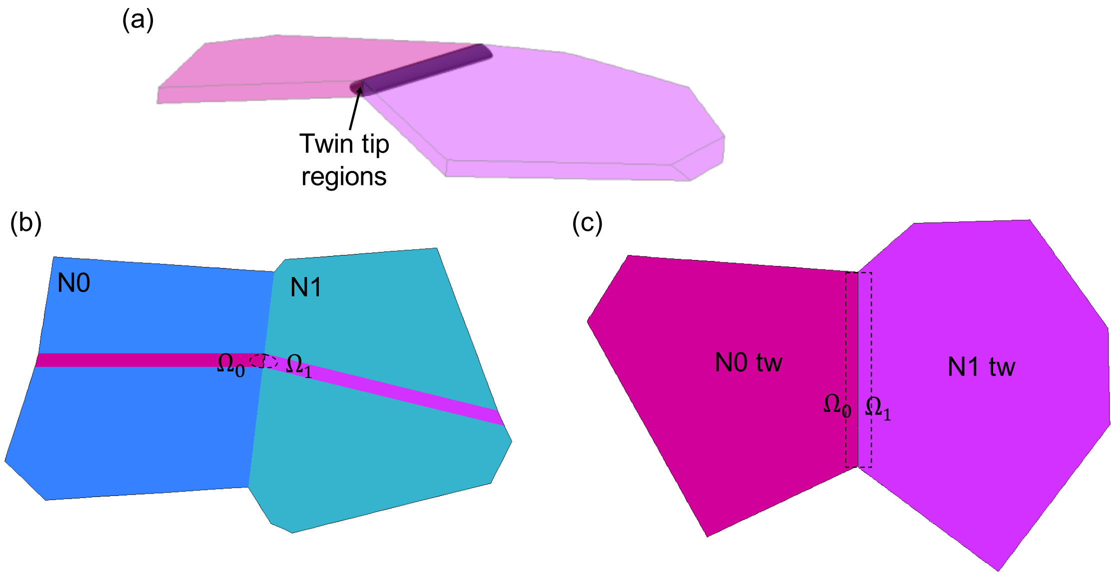

Figure 6: Definition of twin tip regions. (a) 3D structure showing the ATP and the twin tip region. The twin tip regions at the boundary of grains N0 and N1 are contoured by dashed lines in the twin edge view (b) and twin planes view (c). .

Table 4: Lattice orientations of the central grains, and tensile loading directions (in the macroscopic coordinate system) used for the FE simulations. The Schmid factors of the prescribed twin variant are computed using the macroscopic stress.

	Euler angles N0	Euler angles N1	Tensile axis	SF_{N0}	SF_{N1}
$\vec{b}_{tw} \times \vec{n}_{tw}$ type	[277.7 87.0 271.4]	[278.3 77.3 261.6]	[0.73 -0.58 -0.36]	0.5	0.44
$\vec{b}_{tw}$ type	[212.5 68.4 352.3]	[209.1 55.7 358.1]	[0.10 -0.94 0.33]	0.5	0.49

linear intersection of the two twin planes. Grains N0 and N1 thus had a lattice misorientation around $\vec{b}_{tw} \times \vec{n}_{tw}$. In the second simulation ($\vec{b}_{tw}$ type), $\vec{b}_{tw}$ was parallel to the linear intersection of the two twin planes, i.e. grains N0 and N1 thus had a misorientation around $\vec{b}_{tw}$. The Euler angles (Bunge convention) defining the lattice orientations are listed in Table 4, which provides also the macroscopic tensile direction and the Schmid factor for twinning. In both grains, the active twin variant is $(\bar{2}3\bar{3})$ $[31\bar{1}]$.

The simulation results for the ATP of $\vec{b}_{tw} \times \vec{n}_{tw}$ type are shown in Fig. 7. In this figure, the scalar value measuring the amplitude of internal stresses is the resolved shear stress on the active twin variant, which we denote τ_{tw}. For grains N0 and N1, τ_{tw} is expressed in their local coordinate systems, which have an inclination of 13° between each other. τ_{tw} in grain N0 is positive before the onset of twinning and equal to about one half of the macroscopic tensile stress (since the Schmid factor is maximum). The stress field represented in Fig. 7 shows the difference of τ_{tw} before and after imposing the local shear strain inside the twin lamella, noted as $\Delta\tau_{tw}$. Negative values are predicted mostly inside the twin lamella of grain N0, corresponding to so-called back-stresses. In the absence of twin transmission, very large back-stresses are

Table 5: Variation of the internal stresses as a result of twinning. $\langle\Delta\tau_{tw}\rangle_{TwN0}$ means average resolved shear stress for twinning computed inside the whole incoming twin, whereas $\langle\Delta\tau_{tw}\rangle_{\Omega_0}$ and $\langle\Delta\tau_{tw}\rangle_{\Omega_1}$ refer to the two twin tip regions on either sides of the grain boundary.

	$\langle\Delta\tau_{tw}\rangle_{TwN0}$		$\langle\Delta\tau_{tw}\rangle_{\Omega_0}$		$\langle\Delta\tau_{tw}\rangle_{\Omega_1}$	
Transmission:	no	yes	no	yes	no	yes
$\vec{b}_{tw} \times \vec{n}_{tw}$ type	$-3.5\tau_c$	$-3.2\tau_c$	$-4.1\tau_c$	$-3.6\tau_c$	$0.24\tau_c$	$-1.9\tau_c$
$\vec{b}_{tw}$ type	$-3.4\tau_c$	$-3.2\tau_c$	$-4.7\tau_c$	$-2.8\tau_c$	$0.25\tau_c$	$-2.8\tau_c$

observed near the twin tip region in grain N0. If twin transmission occurs, i.e. if the twinning shear strain is enforced also within the lamella of grain N1, the stress concentration at the adjoining twin tip is reduced. The average values of $\Delta\tau_{tw}$ for the entire incoming twin lamella and for the twin tip region Ω_0 are listed in Table 5. For $\vec{b}_{tw} \times \vec{n}_{tw}$ type, the average value of $\Delta\tau_{tw}$ at the twin tip region Ω_0 after twin transmission is still lower than that of the entire twin because of a very thin stress concentration layer near the twin edge (see Fig. 7d) due to the difference of the twin shear strain tensors of the incoming and transmitted twins. For grain N1, $\Delta\tau_{tw}$ is positive before twin transmission, corresponding to forward-stresses that are likely to promote twinning in this adjacent grain. With twin transmission, back-stresses are observed in the transmitted twin, but no large stress concentration is observed at the twin tip region Ω_1.

The simulation results for $\vec{b}_{tw}$ type are shown in Fig. 8. They are qualitatively similar to the prediction of internal stresses for the $\vec{b}_{tw} \times \vec{n}_{tw}$ type. For $\vec{b}_{tw}$ type, without twin transmission, the stress concentration at the twin tip region Ω_0 is even larger than the one for $\vec{b}_{tw} \times \vec{n}_{tw}$ type. However, with twin transmission, $\Delta\tau_{tw}$ at twin tip region becomes similar to the level at the central part of the twin. In other words, the stress concentration at the adjoining twin tip is more significantly reduced via twin transmission for the $\vec{b}_{tw}$ type. It is noteworthy that, in the twin edge view, the twin shear direction is now out of the plane.

4. Discussion

4.1. Favorable conditions for twin transmission

The analysis of crystal orientation maps allows identifying favorable conditions for the transmission of mechanical twins across grain boundaries. ATPs were formed systematically whenever the following two conditions were met simultaneously: both twins have a large Schmid factor for twinning and the two twins have a high geometrical compatibility factor $m' = (\vec{b}_{tw} \cdot \vec{b}'_{tw})(\vec{n}_{tw} \cdot \vec{n}'_{tw})$. Whereas previous works on this question considered hcp metals (Wang et al., 2010b; Barnett et al., 2012; Xin et al., 2015), the present experimental observations tend to indicate that the m' parameter is relevant also in bcc crystals. ATP were

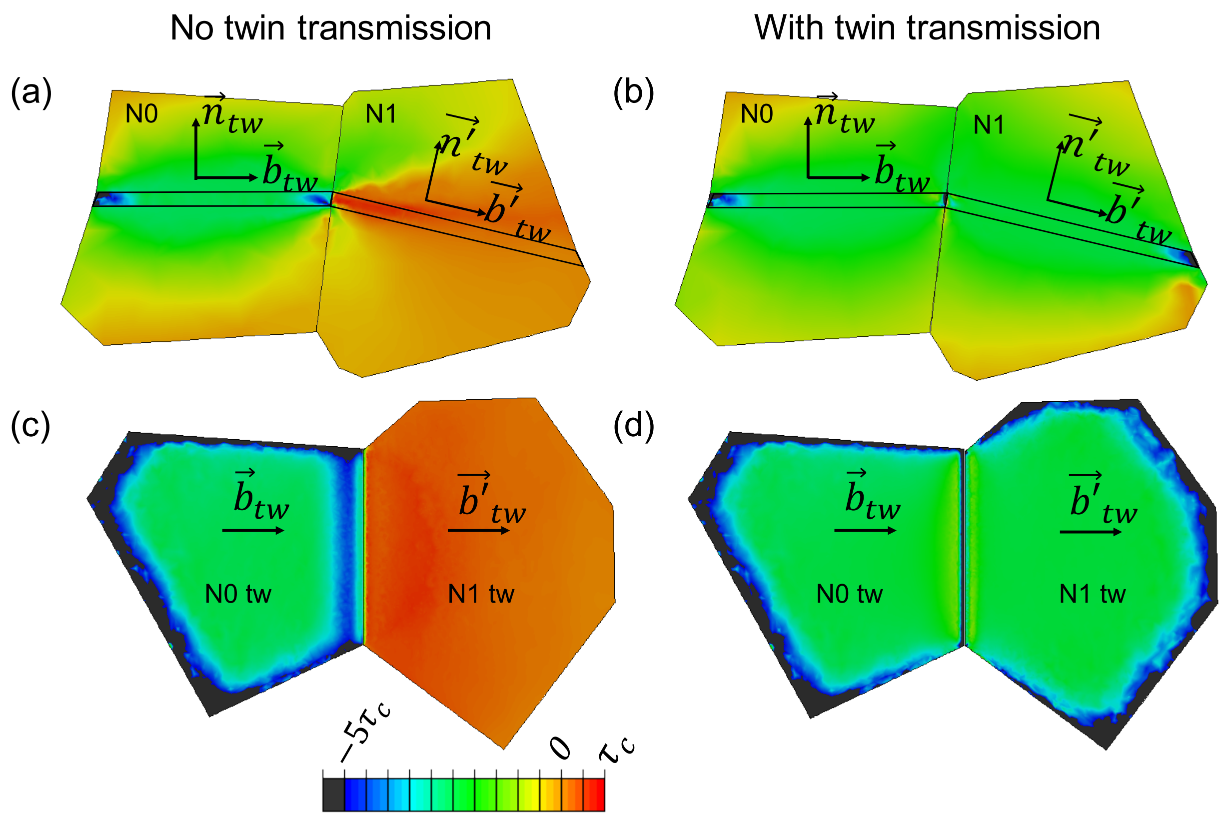

Figure 7: Internal stresses induced by twinning when the misorientation of adjacent grains is around $\vec{b}_{tw} \times \vec{n}_{tw}$. The resolved shear stress τ_{tw} accounts for the local orientation of the twin. The coloring is according to the variation $\Delta\tau_{tw}$ that occurs as a result of the twinning transformation strain. The twin lamella is considered to be transmitted in (b) and (d), but not in (a) and (c). The twin edge view (a,b) and the twin planes view (c,d) are defined in Fig. 6.

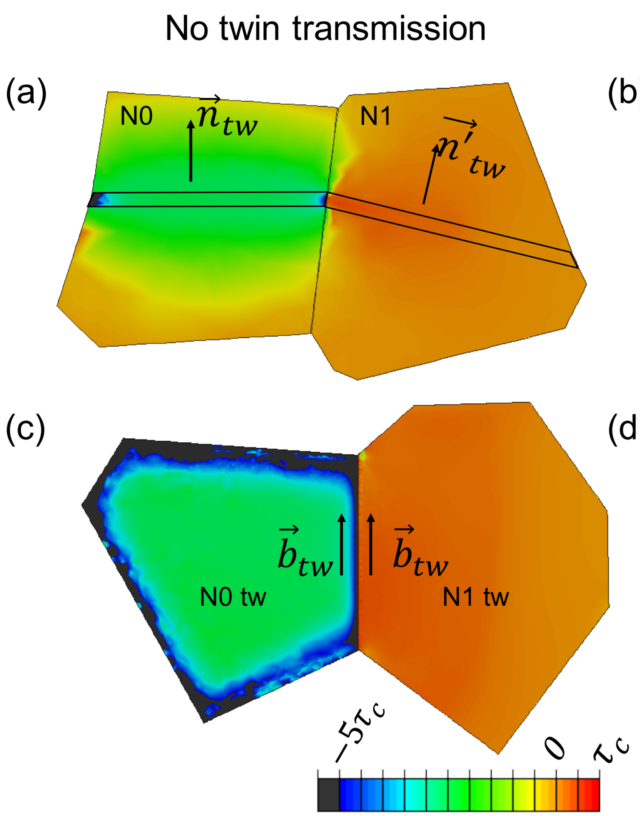

Figure 8: Internal stresses induced by twinning when the misorientation of adjacent grains is around $\vec{b}_{tw}$. The resolved shear stress τ_{tw} accounts for the local orientation of the twin. The coloring is according to the variation $\Delta\tau_{tw}$ that occurs as a result of the twinning transformation strain. The twin lamella is considered to be transmitted in (b) and (d), but not in (a) and (c). The twin edge view (a,b) and the twin planes view (c,d) are defined in Fig. 6.

formed whenever $m' > 0.9$, on the condition that the adjacent grains also have large Schmid factors for twinning. As reported in Table 2, occasional transmission was observed across those grain boundaries where the m' parameter and the Schmid factor had lower values.

The present study also emphasizes another condition for the transmission of a thin twin lamella: the linear intersection of the incoming and transmitted twin planes must lie inside the grain boundary. This condition cannot be assessed directly on a 2D section of the microstructure. However, when all twin lamellae impinging a grain boundary are observed to be transmitted into the adjacent grain, it is most likely that ATP extend in 3D outside the section that has been probed by EBSD. In practice, the intersection of the two twin planes does not lie exactly within the grain boundary if it is computed based on the average orientations of the two grains. In case of misalignment, line contact (point contact in 2D) may still be fulfilled owing to a curvature of the transmitted twin lamella in the vicinity of the grain boundary as demonstrated in Fig. 4. The twin lamella adopts the $\{332\}$ habit plane at a small distance away from the grain boundary. The difference between the energies of coherent and incoherent twin boundaries determines the likeliness of such deviations and hence the chances to form adjoining twin pairs. For fcc material, the coherent $\{111\}$ twin boundary energy is very low. Wolf et al. (1990) calculated twin boundary energy for copper using the embedded atom method, and reported that the boundary energy increased from 9 mJ/m^2 for a coherent twin boundary to 186 mJ/m^2 when the boundary plane deviates from the coherent twin plane by a 13.3° rotation around $[01\bar{1}]$. Such a significant increase of boundary energy makes it energetically unfavorable to deviate from a coherent twin boundary, which may explain why twin transmission seldom occurs in fcc materials. In contrast, the difference between coherent and incoherent twin boundaries is less significant for hcp materials (Wang and Beyerlein, 2012), in which more frequent twin transmission across grain boundaries has been reported. The present experimental data obtained on a bcc material show that 10° misalignment can be compensated. However, the energy of $\{332\}$ twin boundaries in this Ti alloy is yet unknown.

Most of the previously published numerical investigations of twin transmission were performed in 2D or quasi-2D conditions. In such cases, the two twin planes and the grain boundary are all perpendicular to the 2D microstructure section, whereas the direction of the twin shear (in both grains) lies within the section. The misorientation of the two grains is hence around $\vec{b}_{tw} \times \vec{n}_{tw}$ in all 2D simulations. Only recently, Liu et al. (2016) simulated the lateral propagation of a $\{10\bar{1}2\}$ twin in Mg using molecular dynamics simulations, and suggested that such propagation may also contribute to the increase of the twin volume.

For different reasons, we believe that misorientation around $\vec{b}_{tw} \times \vec{n}_{tw}$ is not the most common condition of twin transmission, certainly not in the present bcc material.

- First, we note that the value of m' is not maximized when the misorientation axis is $\vec{b}_{tw} \times \vec{n}_{tw}$. Indeed, the latter situation implies that the two twin planes and the two twin shear directions have the same misalignment, i.e. $\theta_n = \theta_b$, and hence $m' = \cos(\theta_n)^2 = \cos(\theta_b)^2 = \cos(\theta)^2$. The same lattice misorientation around $\vec{b}_{tw}$ or around $\vec{n}_{tw}$ rather leads to $m' = cos(\theta)$ which is larger and hence more in favor of twin transmission.

- Finite element modeling of the internal stresses developed at the edge of a twin lamella provides a second reason why twin transmission is more likely across boundaries hosting misorientations around $\vec{n}_{tw}$ or $\vec{b}_{tw}$. The simulation results reported in Fig. 9 were obtained by impeding plastic relaxation so that the localized shear inside the twin lamella was accommodated elastically by the surrounding. The simulation was repeated while progressively increasing the misorientation of the adjacent grain. Twinning induces a back-stress $\langle \delta\tau_{tw} \rangle_{\Omega_0}$ at the tip of the twin lamella which is to some extent balanced by a forward-stress $\langle \delta\tau_{tw} \rangle_{\Omega_1}$ in the adjacent grain. The forward stress, which is likely to promote twinning in the adjacent grain, is found to decrease when the lattice misorientation increases. The latter decrease is much faster when the misorientation is around $\vec{b}_{tw} \times \vec{n}_{tw}$ than in the other two simulations.

- The inclination of the grain boundary with regard to the twin planes also influences the forward- and back-stresses. Supplementary FE simulations were carried out assuming a disk shaped twin lamella embedded in an elastically isotropic medium. In Fig. 10, α_1 is the angle between $\vec{b}_{tw}$ and the projection of the normal of the grain boundary on the twin plane, and α_2 is the angle between $\vec{n}_{tw}$ and the grain boundary plane. The tubular twin tip regions, denoted Ω_0 and Ω_1 inside and outside the disk, are defined similarly to those presented in Fig. 6. When $\alpha_1 \simeq 0°$, i.e. when the misorientation with the adjacent grain is around $\vec{b}_{tw} \times \vec{n}_{tw}$ (Fig. 3), the grain boundary inclination has hardly any influence on $\langle \delta\tau_{tw} \rangle_{\Omega_0}$ and $\langle \delta\tau_{tw} \rangle_{\Omega_1}$. The predictions vary much more when $\alpha_1 \simeq 90°$, i.e. when the lattice misorientation is around $\vec{b}_{tw}$ or $\vec{n}_{tw}$. Large internal stresses are then developed especially if the boundary plane is perpendicular to the disk plane ($\alpha_2 = 0$). We may thus expect that, when α_2 is less than about 45°, the forward stresses are large enough to trigger twinning in the adjacent grain only if the misalignment of incoming and transmitted twins is around $\vec{b}_{tw}$ or $\vec{n}_{tw}$. Predictions are qualitatively similar when elasticity is anisotropic.

- In the analysis of the microstructure of the β titanium deformed under tension, there is up to now one experimental observation indicating that misorientations around $\vec{b}_{tw}$ may favor twin transmission. In Table 2, the three grain boundaries Gr1/Gr3, Gr16/Gr17 and Gr8/Gr4 all host rather large misorien-

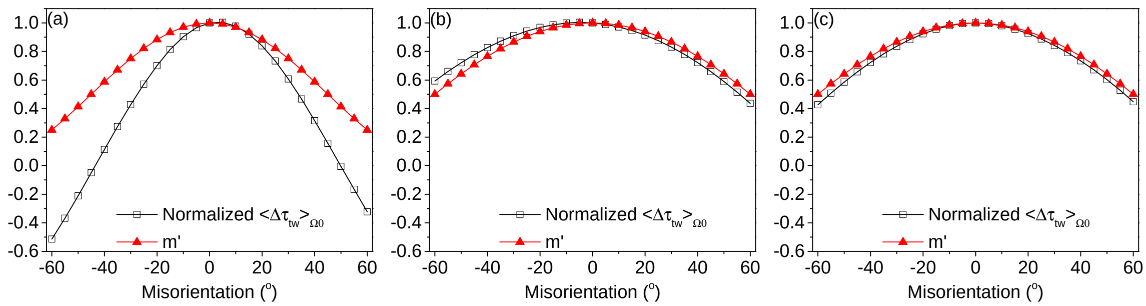

Figure 9: Normalized forward-stresses as a function of the misorientation angle occurring around (a) $\vec{b}_{tw} \times \vec{n}_{tw}$, (b) $\vec{b}_{tw}$, (c) $\vec{n}_{tw}$. For each type of misorientation axis, $\langle \delta\tau_{tw} \rangle_{\Omega_1}$ is normalized by its value when the misorientation angle is zero. The m' value of the incoming and transmitted twins is also plotted.

tation angles $\sim 20°$. However, the misorientation axis at grain boundary Gr1/Gr3 is close to $\vec{b}_{tw}$ (since $\theta_b \ll \theta_n$) and twin transmission is systematic. The misorientation axes at grain boundaries Gr16/Gr17 and Gr8/Gr4 are close to $\vec{b}_{tw} \times \vec{n}_{tw}$ (since $\theta_b \simeq \theta_n$) and twin transmission is occasional. When the misorientation angle is lower than about $10°$, twin transmission is observed whatever the misorientation axis. The orientation map analyzed in the Appendix confirms this trend: when the grain misorientation angle is in the range $10° - 20°$, twin transmission is more probable if the misorientation axis is around either $\vec{b}_{tw}$ or $\vec{n}_{tw}$.

The latter analysis is based on the internal stresses computed from continuum mechanics simulations and on experimental observations having insufficient spatial resolution to reveal the fine scale topology of the ATP. At lower scales, other important parameters are expected to influence twin transmission across grain boundaries. Wang et al. (2010a) performed molecular dynamics simulations of the nucleation of twins at a grain boundary in Mg, demonstrating that low angle, symmetric tilt boundaries are favorable for twin transmission. Twin nucleation clearly is beyond the scope of the present study relying on CPFEM and (2D) orientation maps.

4.2. *Effect of twin transmission on internal stresses*

Elaborate CPFEM simulations of the development of internal stresses in a 3D polycrystalline microstructure were presented in Section 3.2. ATPs corresponding to misorientations around either $\vec{b}_{tw} \times \vec{n}_{tw}$ or $\vec{b}_{tw}$ were considered and the internal stresses, especially nearby the twin tip, were significantly reduced when twin transmission occurred. This phenomenon is likely to influence the macroscopic mechanical response. Indeed, the macroscopic stress is raised when back-stresses develop at the edges of twin lamellae. The present numerical simulations indicate that twin transmission contributes more effectively to the relaxation of such back-stresses than dislocation slip in the adjacent grain.

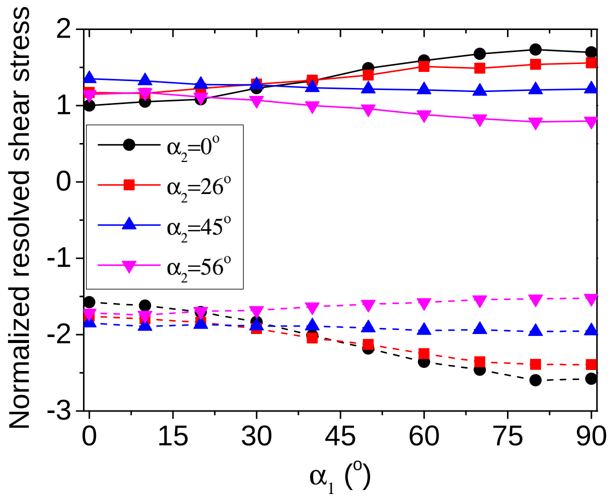

Figure 10: Normalized forward- and back-stresses at the twin tip regions as a function of the inclination of grain boundary. The forward stresses $\langle \delta\tau_{tw} \rangle_{\Omega_1}$ are presented as solid lines, and the back-stresses $\langle \delta\tau_{tw} \rangle_{\Omega_0}$ as dashed lines. Both are normalized by the value of $\langle \delta\tau_{tw} \rangle_{\Omega_1}$ when $\alpha_1 = \alpha_2 = 0$. The definition of α_1 and α_2 are shown in the disk.

This trend is consistent with experimental observations. It has been suggested by Zhang et al. (2008) and Kumar et al. (2015) that the strong back-stress at a twin tip is partly responsible for the lenticular shape of twin lamellae. The RSS for twinning (τ_{tw}) is reduced due to the back-stress and this impedes thickening of the lamella at the twin tips. Glide of twinning dislocations is inhibited at the tip more than in the center of the twin lamella. In the present work, the thickness of twins was observed to decrease close to boundaries when the twins were constrained by the grain boundaries, whereas the thickness of twins was almost unchanged when the twins were transmitted across the grain boundaries. This tends to support the idea that twin transmission can largely reduce the back-stress at the twin tip.

In metallic alloys subject to twinning induced plasticity (TWIP) or transformation induced plasticity (TRIP), back-stresses are expected to represent a significant fraction of the observed strengthening during monotonic loading, also leading to a strong Baushinger effect under cyclic loading (Bouaziz et al., 2008). It is noteworthy that back-stresses of various origins contribute to such kinematic hardening of the material. The back-stress of a twin lamella arrested by a grain boundary is one contribution, which is investigated in the present study. Other important sources of back-stresses are the piling up of dislocations against the twin boundaries and the bowing of dislocation loops inside very thin twin lamellae (Gil Sevillano, 2009). The latter back-stresses have no reason to decrease in case of twin transmission across grain boundaries.

5. Conclusion

Experimental observations and 3D finite element simulations of twin transmission across grain boundaries in a metastable β-Ti lead to the following conclusions:

1. Experimentally, twins are systematically transmitted across grains boundaries whenever there is low misalignment of the incoming and transmitted twins, as characterized by a high geometrical compatibility factor m', combined with large Schmid factors for twinning in both grains. When one of the two factors has a lower value, twin transmission is either occasional or absent.
2. Whereas the transmission of thin twin lamellae in theory requires that the two twin planes intersect along a line within the grain boundary, experimental orientation maps show that misalignments of about 10° can be compensated by a deviation of the twin/matrix interface from the coherent $\{332\}$ crystal plane.
3. Twin transmission across grain boundaries relaxes the back-stress at the edge of the twin more than dislocation slip in the adjacent grain does. Experimentally, twin lamellae have lenticular shape when they are arrested at a grain boundary, whereas the twin thickness of transmitted twins is constant. FE simulations of adjoining twin pairs confirm the reduction of back-stresses at the twin edges.
4. 3D FE simulations of adjoining twin pairs allow us to consider adjacent grains with various lattice misorientations. Results show that internal stresses due to twinning are larger when the adjacent grains share a common twinning shear direction ($\vec{b}_{tw}$) than when the lattice misorientation is around $\vec{b}_{tw} \times \vec{n}_{tw}$, which is the situation treated in most of the earlier numerical studies.

Acknowledgements

FXL and LD are mandated by the Belgian National Fund for Scientific Research (FRS-FNRS). Financial support was obtained from the Communauté Française de Belgique (Action de Recherche Concertée n°15/20-066). MM thanks Pr. F. Prima (PSL-IRCP, France) for his numerous advices.

Appendix

The experimental investigation has been pursued on another sample of the same material which underwent somewhat larger elongation (about 8%). After such larger strain, most grains contain twins (and martensite laths), which improves the statistics. Unfortunately, the distorted crystal lattice complicated the

EBSD analysis: the lattice orientation within twin lamellae were seldom indexed. The twin variants were thus deduced manually from the tilt angle of the traces of twin planes, which are best seen in the EBSD band contrast map Fig. A1. The identification of the correct variant was assessed each time the lattice orientation inside the twin could be measured.

According to the analysis of Fig. 2, twin transmission across grain boundaries is almost systematic when the misorientation is less than 10° and it is rare when the misorientation exceeds 20°. This trend is confirmed here. Therefore, the more detailed analysis is performed only on those grain boundaries with misorientations in the range $10 - 20°$. Such grain boundaries are highlighted in the map: boundaries are shown in white when every impinging twin lamella propagates into the adjacent grain, otherwise they are shown in red.

The results are summarized in Table A1, following the same approach as in Section 2.2. Twin transmission occurs systematically through eight boundaries, which hold an m' larger than 0.95. In contrast, most grain boundaries impeding twin transmission have an m' smaller than 0.93. It is noted that among grain boundaries which allow twin transmission, either θ_n or θ_b tend to have small values, whereas the other grain boundaries have similar θ_n and θ_b. This means that the former boundaries host misorientations around $\vec{b}_{tw}$ or $\vec{n}_{tw}$ whereas the grain misorientation is around $\vec{b}_{tw} \times \vec{n}_{tw}$ in the non-transmitting grain boundaries.

Table A1: Misorientations and twin transmission situations across grain boundaries with a misorientation angle between 10° and 20°. The Schmid fator of the incoming and transmitted twins (SF), the geometrical compatibility factor (m') and the angles θ_b and θ_n of misalignment of two twinning systems are also listed. For grain boundaries where the incoming twin is constrained, twin variants in the neighboring grain with the highest m' are listed.

GB	Misorientation	Transmission	SF	m'	θ_n	θ_b
A37/A36	11°	Systematic	0.43/0.39	0.98	2°	11°
A33/A32	11°	Systematic	0.48/0.45	0.97	10°	10°
A13/A14	12°	Systematic	0.47/0.42	0.98	6°	10°
A25/A26	12°	Systematic	0.48/0.46	0.96	11°	11°
A35/A34	13°	Systematic	0.49/0.48	0.97	3°	13°
A10/A12	15°	Systematic	0.48/0.45	0.96	13°	9°
A6/A7	18°	Systematic	0.30/0.12	0.95	5°	18°
A22/A23	19°	Systematic	0.25/0.33	0.95	18°	4°
A24/A23	14°	No	0.48/0.38	0.96	11°	12°
A8/A9	15°	No	0.36/0.31	0.97	14°	4°
A2/A1	17°	No	0.31/0.31	0.92	16°	17°
A20/A9	17°	No	0.31/0.31	0.93	12°	17°
A31/A32	17°	No	0.44/0.27	0.92	17°	16°
A3/A5	18°	No	0.46/0.37	0.93	16°	15°
A10/A11	19°	No	0.46/0.31	0.91	18°	17°
A3/A4	20°	No	0.46/0.23	0.88	20°	20°

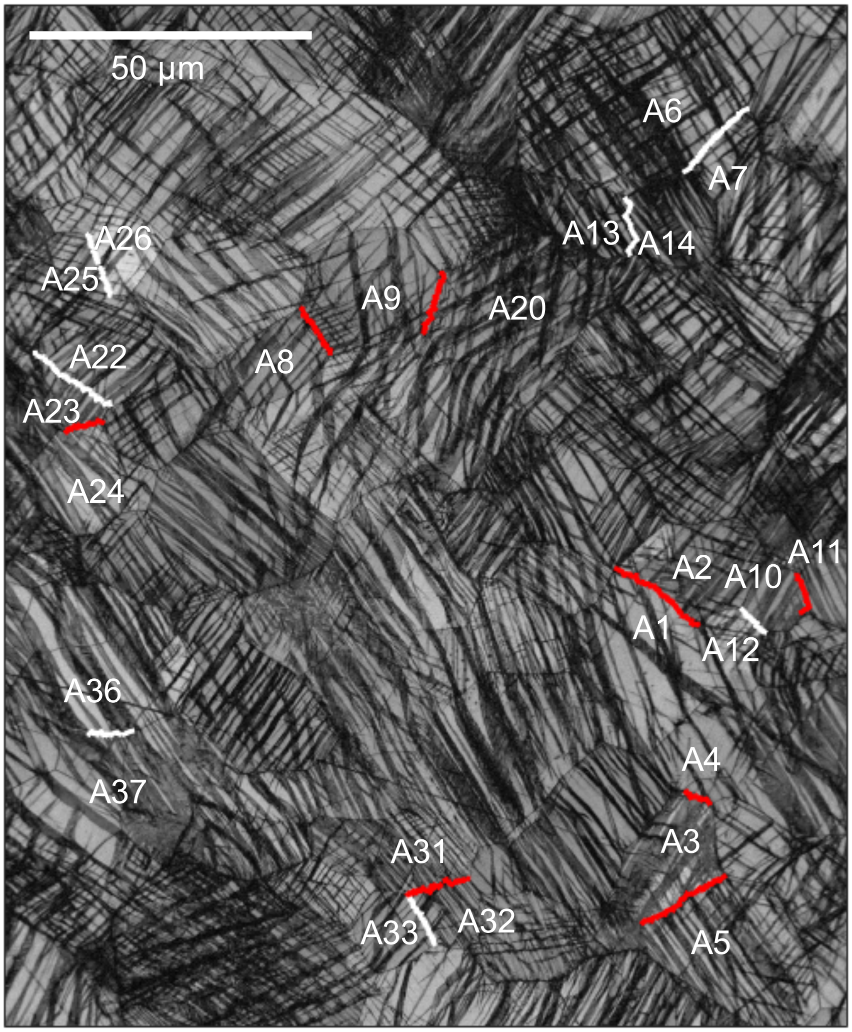

Figure A1: Map of the EBSD band contrast after about 8% elongation of the β-Ti alloy. The tensile direction is horizontal. Grain boundaries with systematic twin transmission are shown in white, and those without systematic twin transmission are shown in red.

References

Abdolvand, H., Daymond, M. R., and Mareau, C. (2011). Incorporation of twinning into a crystal plasticity finite element model: evolution of lattice strains and texture in zircaloy-2. *International Journal of Plasticity*, 27(11):1721–1738.

Abdolvand, H. and Wilkinson, A. J. (2016). On the effects of reorientation and shear transfer during twin formation: comparison between high resolution electron backscatter diffraction experiments and a crystal plasticity finite element model. *International Journal of Plasticity*, 84:160–182.

Ahmed, M., Wexler, D., Casillas, G., Savvakin, D. G., and Pereloma, E. V. (2016). Strain rate dependence of deformation-induced transformation and twinning in a metastable titanium alloy. *Acta Materialia*, 104:190–200.

Amodeo, J., Dancette, S., and Delannay, L. (2016). Atomistically-informed crystal plasticity in mgo polycrystals under pressure. *International Journal of Plasticity*, 82:177–191.

Barnett, M. R., Nave, M. D., and Ghaderi, A. (2012). Yield point elongation due to twinning in a magnesium alloy. *Acta materialia*, 60(4):1433–1443.

Bertrand, E., Castany, P., Péron, I., and Gloriant, T. (2011). Twinning system selection in a metastable β-titanium alloy by schmid factor analysis. *Scripta Materialia*, 64(12):1110–1113.

Beyerlein, I. J., Capolungo, L., Marshall, P. E., McCabe, R. J., and Tomé, C. N. (2010). Statistical analyses of deformation twinning in magnesium. *Philosophical Magazine*, 90(16):2161–2190.

Bouaziz, O., Allain, S., and Scott, C. (2008). Effect of grain and twin boundaries on the hardening mechanisms of twinning-induced plasticity steels. *Scripta Materialia*, 58(6):484–487.

Castany, P., Yang, Y., Bertrand, E., and Gloriant, T. (2016). Reversion of a parent $\{130\}< 310>$ α martensitic twinning system at the origin of $\{332\}< 113>$ β twins observed in metastable β titanium alloys. *Physical Review Letters*, 117(24):245501.

Cheng, J. and Ghosh, S. (2015). A crystal plasticity fe model for deformation with twin nucleation in magnesium alloys. *International Journal of Plasticity*, 67:148–170.

Christian, J. W. and Mahajan, S. (1995). Deformation twinning. *Progress in materials science*, 39(1-2):1–157.

Clausen, B., Tomé, C. N., Brown, D. W., and Agnew, S. R. (2008). Reorientation and stress relaxation due to twinning: modeling and experimental characterization for mg. *Acta Materialia*, 56(11):2456–2468.

Dancette, S., Delannay, L., Renard, K., Melchior, M. A., and Jacques, P. J. (2012). Crystal plasticity modeling of texture development and hardening in twip steels. *Acta Materialia*, 60(5):2135–2145.

Delannay, L., Melchior, M. A., Signorelli, J. W., Remacle, J.-F., and Kuwabara, T. (2009). Influence of grain shape on the planar anisotropy of rolled steel sheets–evaluation of three models. *Computational Materials Science*, 45(3):739–743.

Gil Sevillano, J. (2009). An alternative model for the strain hardening of fcc alloys that twin, validated for twinning-induced plasticity steel. *Scripta Materialia*, 60(5):336–339.

Grosdidier, T. and Philippe, M.-J. (2000). Deformation induced martensite and superelasticity in a β-metastable titanium alloy. *Materials Science and Engineering: A*, 291(1):218–223.

Hielscher, R. and Schaeben, H. (2008). A novel pole figure inversion method: specification of the mtex algorithm. *Journal of Applied Crystallography*, 41(6):1024–1037.

Hölscher, M., Raabe, D., and Lücke, K. (1991). Rolling and recrystallization textures of bcc steels. *steel research international*, 62(12):567–575.

Hutchinson, J. W. (1977). Creep and plasticity of hexagonal polycrystals as related to single crystal slip. *Metallurgical and Materials Transactions A*, 8(9):1465–1469.

Juan, P.-A., Berbenni, S., Barnett, M. R., Tomé, C. N., and Capolungo, L. (2014). A double inclusion homogenization scheme for polycrystals with hierarchal topologies: application to twinning in mg alloys. *International Journal of Plasticity*, 60:182–196.

Kalidindi, S. R. (1998). Incorporation of deformation twinning in crystal plasticity models. *Journal of the Mechanics and Physics of Solids*, 46(2):267273–271290.

Kowalski, N., Delannay, L., Yan, P., and Remacle, J.-F. (2016). Finite element modeling of periodic polycrystalline aggregates with intergranular cracks. *International Journal of Solids and Structures*, 90:60–68.

Kumar, M. A., Beyerlein, I. J., McCabe, R. J., and Tome, C. N. (2016a). Grain neighbour effects on twin transmission in hexagonal close-packed materials. *Nature communications*, 7.

Kumar, M. A., Beyerlein, I. J., and Tomé, C. N. (2016b). Effect of local stress fields on twin characteristics in hcp metals. *Acta Materialia*, 116:143–154.

Kumar, M. A., Kanjarla, A. K., Niezgoda, S. R., Lebensohn, R. A., and Tomé, C. N. (2015). Numerical study of the stress state of a deformation twin in magnesium. *Acta Materialia*, 84:349–358.

Lai, M. J., Tasan, C. C., and Raabe, D. (2016). On the mechanism of $\{332\}$ twinning in metastable β titanium alloys. *Acta Materialia*, 111:173–186.

Leffers, T. and Ray, R. K. (2009). The brass-type texture and its deviation from the copper-type texture. *Progress in Materials Science*, 54(3):351–396.

Lin, F. X., Zhang, Y. B., Pantleon, W., and Juul Jensen, D. (2015). Supercube grains leading to a strong cube texture and a broad grain size distribution after recrystallization. *Philosophical Magazine*, 95(22):2427–2449.

Liu, Y., Li, N., Shao, S., Gong, M., Wang, J., McCabe, R., Jiang, Y., and Tomé, C. N. (2016). Characterizing the boundary lateral to the shear direction of deformation twins in magnesium. *Nature communications*, 7.

Luster, J. and Morris, M. (1995). Compatibility of deformation in two-phase ti-al alloys: Dependence on microstructure and orientation relationships. *Metallurgical and Materials Transactions A*, 26(7):1745–1756.

Mareau, C. and Daymond, M. R. (2016). Micromechanical modelling of twinning in polycrystalline materials: Application to magnesium. *International Journal of Plasticity*, 85:156–171.

Marteleur, M., Sun, F., Gloriant, T., Vermaut, P., Jacques, P. J., and Prima, F. (2012). On the design of new β-metastable titanium alloys with improved work hardening rate thanks to simultaneous trip and twip effects. *Scripta Materialia*, 66(10):749–752.

Meyers, M. A., Vöhringer, O., and Lubarda, V. A. (2001). The onset of twinning in metals: a constitutive description. *Acta materialia*, 49(19):4025–4039.

Min, X. H., Tsuzaki, K., Emura, S., Sawaguchi, T., Ii, S., and Tsuchiya, K. (2013). {332}< 113> twinning system selection in a β-type ti–15mo–5zr polycrystalline alloy. *Materials Science and Engineering: A*, 579:164–169.

Proust, G., Tomé, C. N., and Kaschner, G. C. (2007). Modeling texture, twinning and hardening evolution during deformation of hexagonal materials. *Acta Materialia*, 55(6):2137–2148.

Rohrer, G., Li, J., Lee, S., Rollett, A., Groeber, M., and Uchic, M. (2010). Deriving grain boundary character distributions and relative grain boundary energies from three-dimensional ebsd data. *Materials Science and Technology*, 26(6):661–669.

Salem, A. A., Kalidindi, S. R., and Semiatin, S. L. (2005). Strain hardening due to deformation twinning in α-titanium: Constitutive relations and crystal-plasticity modeling. *Acta Materialia*, 53(12):3495–3502.

Sander, B. and Raabe, D. (2008). Texture inhomogeneity in a ti–nb-based β-titanium alloy after warm rolling and recrystallization. *Materials Science and Engineering: A*, 479(1):236–247.

Siska, F., Stratil, L., Cizek, J., Ghaderi, A., and Barnett, M. R. (2017). Numerical analysis of twin thickening process in magnesium alloys. *Acta Materialia*, 124:9–16.

Sun, F., Zhang, J. Y., Marteleur, M., Brozek, C., Rauch, E., Veron, M., Vermaut, P., Jacques, P. J., and Prima, F. (2015). A new titanium alloy with a combination of high strength, high strain hardening and improved ductility. *Scripta Materialia*, 94:17–20.

Sun, F., Zhang, J. Y., Marteleur, M., Gloriant, T., Vermaut, P., Laillé, D., Castany, P., Curfs, C., Jacques, P. J., and Prima, F. (2013). Investigation of early stage deformation mechanisms in a metastable β titanium alloy showing combined twinning-induced plasticity and transformation-induced plasticity effects. *Acta Materialia*, 61(17):6406–6417.

Tobe, H., Kim, H. Y., Inamura, T., Hosoda, H., and Miyazaki, S. (2014). Origin of {332} twinning in metastable β-ti alloys. *Acta materialia*, 64:345–355.

Tomé, C. N., Lebensohn, R. A., and Kocks, U. F. (1991). A model for texture development dominated by deformation twinning: application to zirconium alloys. *Acta metallurgica et materialia*, 39(11):2667–2680.

Van Houtte, P. (1978). Simulation of the rolling and shear texture of brass by the taylor theory adapted for mechanical twinning. *Acta Metallurgica*, 26(4):591–604.

Wang, J., Beyerlein, I., and Tomé, C. (2010a). An atomic and probabilistic perspective on twin nucleation in mg. *Scripta Materialia*, 63(7):741–746.

Wang, J. and Beyerlein, I. J. (2012). Atomic structures of symmetric tilt grain boundaries in hexagonal close packed (hcp) crystals. *Modelling and Simulation in Materials Science and Engineering*, 20(2):024002.

Wang, L., Eisenlohr, P., Yang, Y., Bieler, T. R., and Crimp, M. A. (2010b). Nucleation of paired twins at grain boundaries in titanium. *Scripta Materialia*, 63(8):827–830.

Welsch, G., Boyer, R., and Collings, E. W. (1993). *Materials properties handbook: titanium alloys*. ASM international.

Wolf, U., Gumbsch, P., Ichinose, H., and Fischmeister, H. F. (1990). Incoherent σ3 grain boundaries in fcc metals: The influence of inclination on the boundary structure and energy. *Le Journal de Physique Colloques*, 51(C1):C1–359.

Wong, S. L., Madivala, M., Prahl, U., Roters, F., and Raabe, D. (2016). A crystal plasticity model for twinning- and transformation-induced plasticity. *Acta Materialia*, 118:140–151.

Xin, R., Liang, Y., Ding, C., Guo, C., Wang, B., and Liu, Q. (2015). Geometrical compatibility factor analysis of paired extension twins in extruded mg–3al–1zn alloys. *Materials & Design*, 86:656–663.

Yang, F., Yin, S. M., Li, S. X., and Zhang, Z. F. (2008). Crack initiation mechanism of extruded az31 magnesium alloy in the very high cycle fatigue regime. *Materials Science and Engineering: A*, 491(1):131–136.

Yin, S. M., Yang, F., Yang, X. M., Wu, S. D., Li, S. X., and Li, G. Y. (2008). The role of twinning–detwinning on fatigue fracture morphology of mg–3% al–1% zn alloy. *Materials Science and Engineering: A*, 494(1):397–400.

Zhang, R. Y., Daymond, M. R., and Holt, R. A. (2008). A finite element model of deformation twinning in zirconium. *Materials Science and Engineering: A*, 473(1):139–146.